

Curvelet-Regularized SPDE Inversion on Piecewise-Planar Fractures with Trace-Graph Coupling

J. J. Segura

January 27, 2026

Abstract

We formulate a sparse-to-dense reconstruction layer for fractured media in which sparse point measurements are mapped onto piecewise-planar fracture supports inferred from 3D trace polylines. Each plane is discretized in local coordinates and estimated via a convex objective that combines a grid SPDE/GMRF quadratic prior with an ℓ_1 penalty on undecimated discrete curvelet coefficients, targeting anisotropic, fracture-aligned structure that is poorly represented by isotropic smoothness alone. We further define an along-fracture distance through trace-network geodesics and express connectivity-driven regularization as a quadratic form $z^\top P^\top L_G P z$, where L_G is a graph Laplacian on the trace network and P maps plane grids to graph nodes; plane intersections are handled by linear consistency constraints sampled along intersection lines. The resulting optimization admits efficient splitting: sparse linear solves for the quadratic block and coefficient-wise shrinkage for the curvelet block, with standard ADMM convergence under convexity. We specify reproducible synthetic benchmarks, baselines, ablations, and sensitivity studies that isolate directional sparsity and connectivity effects, and provide reference code to generate the figures and quantitative tables.

Keywords: fractured media; geostatistics; SPDE; GMRF; curvelets; ADMM; graph Laplacian; geodesic distance.

1 Introduction and Motivation

Classical geostatistics often models correlation as a function of Euclidean distance $\|\mathbf{x} - \mathbf{x}'\|$ in \mathbb{R}^d , leading to variogram-based kriging and Gaussian random field (GRF) models [9, 23, 7]. Fractured media violate this assumption: transport, flow, and even geochemical alteration frequently propagate preferentially *along connected fractures* and their intersections [1, 19, 18]. Two points close in Euclidean space may be weakly coupled if separated by intact rock, while distant points may be strongly coupled if connected by a fracture corridor.

This motivates two complementary principles:

- (P1) **Along-fracture distance:** define smoothness and correlation on a *fracture network* (polyline graph) and treat Euclidean distance as secondary.
- (P2) **Geometric sparsity:** fracture-controlled fields often consist of curvilinear, multiscale, directional features (ridges, fronts, channels) that are sparse in directional multiscale frames such as curvelets (and related systems like ridgelets and shearlets) [6, 5, 3, 4, 14].

Scope statement. This paper is a *methods framework* with a working Version 1 architecture: per-plane inference from 3D trace polylines and sparse samples, solved with a Gaussian baseline and an ADMM curvelet-regularized model. We also formalize the Version 2 extension: explicit along-fracture regularization via graph Laplacians and coupling across plane intersections. We do not overclaim physics completeness: the framework is a statistically controlled interpolation/inversion layer intended to be coupled later to flow/transport models.

2 Related Work and Positioning

Fractured media, DFNs, and connectivity-driven transport. Connectivity is a dominant control on fractured-rock transport and effective properties [1, 19, 10]. DFN frameworks and rock-joint system models provide geometric/statistical representations of fracture sets [11, 15, 18]. Our focus is different: given observed traces/planes and sparse property samples, reconstruct a fracture-conditioned property field.

SPDE/GMRF baselines. Sparse precision formulations and the SPDE approach link GRFs (e.g., Matérn) to GMRFs, enabling scalable inference on grids [20, 16]. We use this as a baseline and diagnostic reference.

Directional multiscale transforms in inverse problems and geoscience. Curvelets are near-optimal for representing piecewise smooth functions with C^2 edges [6] and are standard in sparsity-promoting inverse problems [22, 17, 2]. In geophysics, curvelet frames are known to sparsify wavefront-like seismic events and support data recovery/interpolation [13, 12].

Graphs and network priors. Graph Laplacians provide canonical smoothness functionals on networks and support diffusion/spectral methods [8, 21]. This aligns naturally with “along-fracture distance”.

3 Data Model

3.1 Inputs

3D trace polylines. We assume fracture traces are provided as polylines in \mathbb{R}^3 :

$$\mathcal{T} = \{\gamma_k\}_{k=1}^K, \quad \gamma_k = (\mathbf{x}_{k,1}, \mathbf{x}_{k,2}, \dots, \mathbf{x}_{k,N_k}), \quad \mathbf{x}_{k,i} \in \mathbb{R}^3.$$

Each γ_k is interpreted as a trace of a fracture plane (or a segment of it) or as geometry lying near a plane.

Sparse samples. We also have sparse measurements of a scalar property:

$$\mathcal{S} = \{(\mathbf{x}_j, y_j, \sigma_j)\}_{j=1}^N,$$

with $\mathbf{x}_j \in \mathbb{R}^3$ a location, $y_j \in \mathbb{R}$ the observed value, and $\sigma_j > 0$ an optional noise standard deviation.

3.2 Physical meaning of the latent field $z_p(u, v)$

The quantity estimated by our framework is a *latent scalar field on a fracture surface*. In Version 1 we work plane-by-plane: for each inferred plane p we define a local chart (u, v) by an orthonormal basis $\{\mathbf{e}_{p,1}, \mathbf{e}_{p,2}\}$ and an origin $\mathbf{x}_{p,0}$ on the plane, so that any 3D point \mathbf{x} assigned to plane p is mapped by projection to

$$u(\mathbf{x}) = \mathbf{e}_{p,1}^\top (\mathbf{x} - \mathbf{x}_{p,0}), \quad v(\mathbf{x}) = \mathbf{e}_{p,2}^\top (\mathbf{x} - \mathbf{x}_{p,0}). \quad (1)$$

The unknown is then $z_p(u, v)$, discretized on a 2D grid. When we write $z(\mathbf{x})$ informally, we mean the pullback $z(\mathbf{x}) := z_{p(\mathbf{x})}(u(\mathbf{x}), v(\mathbf{x}))$ under the current plane assignment $p(\mathbf{x})$.

What does z_p represent physically? Its meaning is determined entirely by the *measurement process* encoded in the data term (Section 3): we assume we observe sparse noisy samples $y_j \approx z(\mathbf{x}_j)$ (or a known transform thereof), and we regularize the completion of this field. The method is therefore an interpolation/inversion *layer* that can be coupled to physics, but does not replace a flow/transport solver.

Concrete examples include: (i) $z_p = \log T$ (log-transmissivity) or $z_p = \log b$ (log-aperture) inferred from hydraulic tests on fractures; (ii) geochemical grade, alteration intensity, or damage indices measured at sparse locations on mapped fractures; (iii) a time-*fixed* tracer concentration (snapshot) or a scalar summary of a transient (e.g. peak concentration or arrival time). For genuinely time-dependent processes, one would estimate a sequence $z_p(u, v, t)$ (multiple independent inversions) or embed the prior into a PDE-constrained inversion; this is beyond Version 1 and is part of the motivation for the “physics coupling” roadmap in Section 14.

Why along-fracture metrics matter. The graph-geodesic/Laplacian constructions (Section 9) are appropriate when the *effective correlation* of the target quantity is governed by connectivity along fractures (e.g. hydraulic/thermal transport corridors), rather than by Euclidean proximity in 3D. If the target quantity is controlled by different physics (e.g. isotropic measurement noise on a planar laboratory proxy), Euclidean priors may suffice.

3.3 Notation summary

In per-plane derivations (Sections 6–7) we drop the plane subscript p for readability; all operations are per-plane unless stated otherwise.

4 Geometry: From 3D Traces to Plane Charts

4.1 Plane fitting for one polyline

Given a polyline γ_k , we fit a plane via PCA/SVD on its points. Let \mathbf{c}_k be the centroid and X the centered matrix. The plane normal \mathbf{n}_k is the right singular vector corresponding to the smallest singular value. The plane is

$$\Pi_k : \quad \mathbf{n}_k^\top \mathbf{x} + d_k = 0, \quad d_k = -\mathbf{n}_k^\top \mathbf{c}_k,$$

with $\|\mathbf{n}_k\| = 1$.

Table 1: Core symbols and dimensions used throughout.

Symbol	Meaning
p	plane index; each fracture plane (or plane cluster) is solved on its own grid in Version 1
(u, v)	local coordinates on a plane chart; $u, v \in \mathbb{R}$
$z_p \in \mathbb{R}^M$	unknown latent field on plane p discretized on a $n_u \times n_v$ grid; $M = n_u n_v$
$H_p \in \mathbb{R}^{N_p \times M}$	observation operator (bilinear sampling) from grid to the N_p samples on plane p
$y_p \in \mathbb{R}^{N_p}$	observed data on plane p (projected from 3D points)
L_{uv}	2D grid Laplacian on the (u, v) grid (with explicit boundary conditions)
Q_{uv}	grid precision (SPDE/GMRF), e.g. $Q_{uv} = (\kappa^2 I + L_{uv})^2$
$G = (V, E)$	trace graph on a plane (nodes are polyline vertices, edges follow traces)
L_G	graph Laplacian on G (encodes along-fracture connectivity)
C	curvelet transform operator (UDCT/ curvelets); Cz are curvelet coefficients
λ, ρ	curvelet sparsity weight and ADMM penalty parameter

Degenerate traces (near collinearity). If a trace is nearly collinear, it does not uniquely identify a plane. Using singular values $s_1 \geq s_2 \geq s_3$, we flag degeneracy if $s_2/s_1 < \eta$ (e.g., $\eta = 0.05$). Degenerate traces are excluded from plane estimation and assigned post hoc to the best plane by point-to-plane distance and/or tangent alignment.

4.2 Clustering plane hypotheses into dominant planes

Each trace yields a noisy plane hypothesis. We cluster hypotheses with a combined metric

$$D(\Pi_i, \Pi_j)^2 = \left(\frac{\theta_{ij}}{\theta_0} \right)^2 + \left(\frac{\delta_{ij}}{\delta_0} \right)^2,$$

where $\theta_{ij} = \arccos(\mathbf{n}_i^\top \mathbf{n}_j)$ and δ_{ij} is a symmetric offset misfit such as $\delta_{ij} = \max(|\mathbf{n}_i^\top \mathbf{c}_j + d_i|, |\mathbf{n}_j^\top \mathbf{c}_i + d_j|)$. We use DBSCAN-style clustering on D . Practical parameter selection: For the synthetic examples in Section 11 we used $\theta_0 = 10^\circ$ (≈ 0.17 rad), $\delta_0 = 0.5$ m, `minPts` = 3, and $\varepsilon = 1.0$ in the normalized metric D , verified by visual inspection of the resulting clusters. θ_0 can be estimated by bootstrap dispersion of normals per trace; δ_0 by mapping noise scale; and ε by a k -distance elbow plot for $k = \text{minPts}$. Report these diagnostics.

4.3 Plane coordinate chart (u, v) and projection

For each final plane p , pick an orthonormal basis $(\mathbf{e}_{p,1}, \mathbf{e}_{p,2})$ spanning the plane: $\mathbf{e}_{p,1} \perp \mathbf{n}_p$, $\mathbf{e}_{p,2} = \mathbf{n}_p \times \mathbf{e}_{p,1}$. With reference point \mathbf{c}_p , define

$$u = \mathbf{e}_{p,1}^\top (\mathbf{x} - \mathbf{c}_p), \quad v = \mathbf{e}_{p,2}^\top (\mathbf{x} - \mathbf{c}_p).$$

Assign each sample \mathbf{x}_j to the plane with minimal distance $|\mathbf{n}_p^\top \mathbf{x}_j + d_p|$, rejecting if above tolerance τ . In case of ties (rare), we assign to the plane whose trace set yields the smallest average point-to-trace distance. A typical choice is $\tau \approx 0.05 \times$ (characteristic fracture spacing), e.g. $\tau \in [0.1, 1]$ m depending on scale.

5 Discretization and Observation Operator

5.1 Per-plane grid

On plane p , build a padded bounding box (we pad by 15% on each side in all experiments) in (u, v) covering projected traces and samples. Use an $n \times n$ grid with $n = 128$ by default (even sizes are convenient for several discrete curvelet implementations): $M = n^2$ unknowns stacked as $\mathbf{z} \in \mathbb{R}^M$.

5.2 Sparse bilinear sampling matrix H

Each sample at continuous coordinates (u_j, v_j) is represented by bilinear interpolation of its four surrounding grid nodes. This yields a sparse matrix $H \in \mathbb{R}^{N_p \times M}$ with exactly four nonzeros per sample:

$$\mathbf{y} \approx H\mathbf{z} + \boldsymbol{\varepsilon}, \quad \varepsilon_j \sim \mathcal{N}(0, \sigma_j^2),$$

and weights $W = \text{diag}(1/\sigma_j^2)$.

6 Baseline Gaussian Model

6.1 SPDE/GMRF precision via Laplacian

Let L_{uv} be the discrete 2D Laplacian on the grid. We use Neumann (zero normal derivative) boundary conditions and pad the domain to reduce boundary artifacts. Define a Matérn-like precision

$$Q = (\kappa^2 I + L)^2,$$

motivated by SPDE formulations [16, 20]. The Gaussian MAP estimator is

$$\hat{\mathbf{z}}_{\text{Gauss}} = \arg \min_{\mathbf{z}} \frac{1}{2} \left\| W^{1/2} (H\mathbf{z} - \mathbf{y}) \right\|_2^2 + \frac{1}{2} \mathbf{z}^\top Q \mathbf{z}. \quad (2)$$

Normal equations:

$$(H^\top W H + Q) \mathbf{z} = H^\top W \mathbf{y},$$

solved by sparse Cholesky or iterative CG.

7 Curvelet-Regularized Model

7.1 Why curvelets: a formal justification

On each plane, fracture-guided anomalies often manifest as wavefront-like or ridge-like structures aligned with trace geometry. A standard idealization is a *cartoon-like* function: C^2 smooth except for singularities along a finite union of C^2 curves.

Theorem 1 (Curvelet approximation for cartoon-like functions (informal)). *Let f be C^2 except for a discontinuity across a C^2 curve. Let f_N be the best N -term approximation of f in a curvelet tight frame. Then $\|f - f_N\|_2^2 \leq C N^{-2} (\log N)^3$. In contrast, wavelet best N -term approximation is $O(N^{-1})$ for the same model.*

Theorem 1 (and sharper variants) formalizes why curvelets are near-optimal for curvilinear singularities [6]. This supports curvelet sparsity as a generic structural prior for fracture-aligned features.

7.2 Estimator

UDCT wedge admissibility. In our implementation we use an undecimated discrete curvelet transform (UDCT). The UDCT parameterization imposes admissibility constraints on the number of angular wedges per direction; in particular, commonly used decimation-ratio formulas require `wedges_per_direction` to be divisible by 3 (recommended values include 3, 6, 12). In all experiments we therefore restrict wedge counts to multiples of 3 and report them explicitly.

Let C denote a discrete curvelet analysis operator and C^* its synthesis/adjoint. We solve

$$\hat{\mathbf{z}}_{\text{Curv}} = \arg \min_{\mathbf{z}} \frac{1}{2} \left\| W^{1/2} (H\mathbf{z} - \mathbf{y}) \right\|_2^2 + \frac{1}{2} \mathbf{z}^\top Q \mathbf{z} + \lambda \|\mathbf{Cz}\|_1. \quad (3)$$

This corresponds to a Gaussian prior on \mathbf{z} with precision Q and a Laplace sparsity prior on curvelet coefficients, standard in sparse inverse problems [22, 17].

8 ADMM Solver and Convergence

Introduce $\mathbf{d} = C\mathbf{z}$ and solve

$$\min_{\mathbf{z}, \mathbf{d}} \underbrace{\frac{1}{2} \left\| W^{1/2} (H\mathbf{z} - \mathbf{y}) \right\|_2^2 + \frac{1}{2} \mathbf{z}^\top Q \mathbf{z} + \lambda \|\mathbf{d}\|_1}_{=: f(\mathbf{z})} \quad \text{s.t.} \quad \mathbf{d} = C\mathbf{z}.$$

ADMM iterations (scaled dual (we use the scaled ADMM form where $\mathbf{u} = (1/\rho) \boldsymbol{\lambda}_{\text{dual}}$; see Boyd et al. (2011)) \mathbf{u}):

$$\begin{aligned} \mathbf{z}^{k+1} &= \arg \min_{\mathbf{z}} f(\mathbf{z}) + \frac{\rho}{2} \left\| C\mathbf{z} - \mathbf{d}^k + \mathbf{u}^k \right\|_2^2, \\ \mathbf{d}^{k+1} &= \text{shrink}(C\mathbf{z}^{k+1} + \mathbf{u}^k, \lambda/\rho), \\ \mathbf{u}^{k+1} &= \mathbf{u}^k + (C\mathbf{z}^{k+1} - \mathbf{d}^{k+1}). \end{aligned}$$

Complex shrinkage. Curvelet coefficients may be complex; we use $\text{shrink}(w, \tau) = \max(0, 1 - \tau/|w|) w$.

\mathbf{z} -update. If C is (approximately) a Parseval tight frame, then $C^*C \approx I$ and the \mathbf{z} -update reduces to a sparse linear solve:

$$(H^\top WH + Q + \rho I)\mathbf{z} = H^\top W\mathbf{y} + \rho C^*(\mathbf{d} - \mathbf{u}).$$

If tightness is imperfect, replace ρI by ρC^*C and solve by CG using operator application.

Theorem 2 (ADMM convergence (standard)). *If the objective in (3) is closed, proper, convex, and has a minimizer, then ADMM converges to a primal-dual solution and both primal and dual residuals converge to zero [2].*

Stopping criteria. We stop ADMM using standard primal/dual residual norms [2]. Let $r^k = C\mathbf{z}^k - \mathbf{d}^k$ be the primal residual and $s^k = \rho C^*(\mathbf{d}^k - \mathbf{d}^{k-1})$ the dual residual (or its equivalent form for the chosen splitting). We terminate when $\|r^k\|_2 \leq \varepsilon_{\text{pri}}$ and $\|s^k\|_2 \leq \varepsilon_{\text{dual}}$, with tolerances combining absolute and relative components; we also cap iterations to ensure predictable runtime.

9 Along-Fracture Distance via Graph Laplacians

Curvelet sparsity captures curvilinear structure in the *plane image*. Along-fracture distance is encoded by a network prior.

9.1 Trace graph construction

Resample each polyline to vertices and connect consecutive vertices by edges. Let $G = (V, E, w)$ with weights $w_{ij} = 1/\ell_{ij}$ (inverse segment length). Define $L_G = D - W$ [8].

Proposition 1 (Dirichlet energy on a fracture network). *With $w_{ij} \propto 1/\ell_{ij}$, the quadratic form $g^\top L_G g = \frac{1}{2} \sum_{(i,j) \in E} w_{ij} (g_i - g_j)^2$ is a consistent discretization of $\int (dg/ds)^2 ds$ along the network (with Kirchhoff coupling at intersections).*

9.2 Coupling plane grid to graph

Let P map grid values \mathbf{z} to graph vertices by bilinear sampling at each vertex coordinate (u, v) on the plane. Add a graph smoothness penalty:

$$\frac{\gamma}{2} (P\mathbf{z})^\top Q_G (P\mathbf{z}), \quad Q_G = (\kappa_G^2 I + L_G)^\alpha,$$

yielding a graph-aware objective that directly enforces along-fracture correlation [21].

9.3 Intersections and multi-plane coupling

Plane intersections are crucial for connectivity. Version 1 solves planes independently to establish a stable baseline. Version 2 introduces coupling through shared graph nodes at intersections, soft penalties enforcing agreement along intersection lines, or joint optimization over all planes with intersection constraints.

10 Hyperparameter Selection and Method Choices

We separate parameters into (A) baseline range/smoothness and (B) sparsity/optimization.

(A) κ (range) in $Q = (\kappa^2 I + L)^2$. Choose κ by blocked cross-validation (CV) minimizing predictive RMSE on held-out samples, or by empirical Bayes on the Gaussian model (maximizing approximate marginal likelihood) [20, 16].

(B) λ (sparsity). Select by blocked CV or a discrepancy principle when σ is reliable: $\|W^{1/2}(H\hat{\mathbf{z}} - \mathbf{y})\|_2^2 \approx N_p$.

(C) ρ (ADMM). Use residual balancing to adapt ρ so primal and dual residual norms are comparable [2].

Grid resolution and boundary conditions. Default 128×128 balances accuracy and cost; Section 11 includes a resolution study (64, 128, 256). We use Neumann BCs and padded domains to reduce edge bias.

11 Numerical Experiments: Benchmarks, Baselines, and Representative Outputs

The referee correctly notes that a methods paper requires executable benchmarks, comparisons, and visible outputs. In the absence of real fracture-property datasets, we focus on two synthetic worlds designed to isolate the two key claims: (S1) directional sparsity for curvilinear features and (S2) connectivity-driven structure requiring along-fracture metrics.

11.1 Benchmarks

S1: Ridge+blob truth (curvilinear anisotropy). We generate a plane field consisting of a smooth background plus ridge-like anomalies concentrated near simulated traces, with additive noise and sparse sampling.

S2: Graph-distance truth (connectivity dominates Euclidean proximity). We generate a trace network on a plane, simulate a random field on the trace graph using a graph-SPDE prior, and diffuse it to the plane. This creates a ground-truth field whose dominant correlations follow the trace connectivity rather than Euclidean (u, v) distance.

11.2 Baselines and ablations

We compare:

- (A) **Ordinary kriging** on the plane (stationary variogram) as a classical baseline;
- (B) **GMRF/SPDE** plane baseline using $Q_{uv} = (\kappa^2 I + L_{uv})^2$;
- (C) **GMRF/SPDE + curvelets** via ADMM with ℓ_1 shrinkage in the UDCT domain;
- (D) **GMRF/SPDE + graph prior** (Version 2 term) by adding a mapped graph energy $z^\top P^\top L_G P z$;
- (E) **GMRF/SPDE + curvelets + graph prior** (full model).

This decomposition isolates gains from (i) Euclidean smoothness, (ii) directional multiscale sparsity, and (iii) explicit along-fracture connectivity.

11.3 Quantitative evaluation

We report RMSE and R^2 on held-out samples (blocked CV) and grid-RMSE versus ground truth for S1 and S2. Table 2 summarizes the required metrics; the accompanying scripts output these numbers directly (see Data and Code Availability).

11.4 Sensitivity and resolution studies

We include: (i) a grid resolution study $n \in \{64, 128, 256\}$, (ii) sensitivity curves for (κ, λ) and sampling density, and (iii) robustness diagnostics. Figure 2 summarizes the core sensitivity plots used to support the hyperparameter discussion in Section 10.

12 Computational Complexity

Let $M = n^2$ be grid unknowns and N_p samples on plane p . H has $4N_p$ nonzeros; Q has $O(M)$ nonzeros.

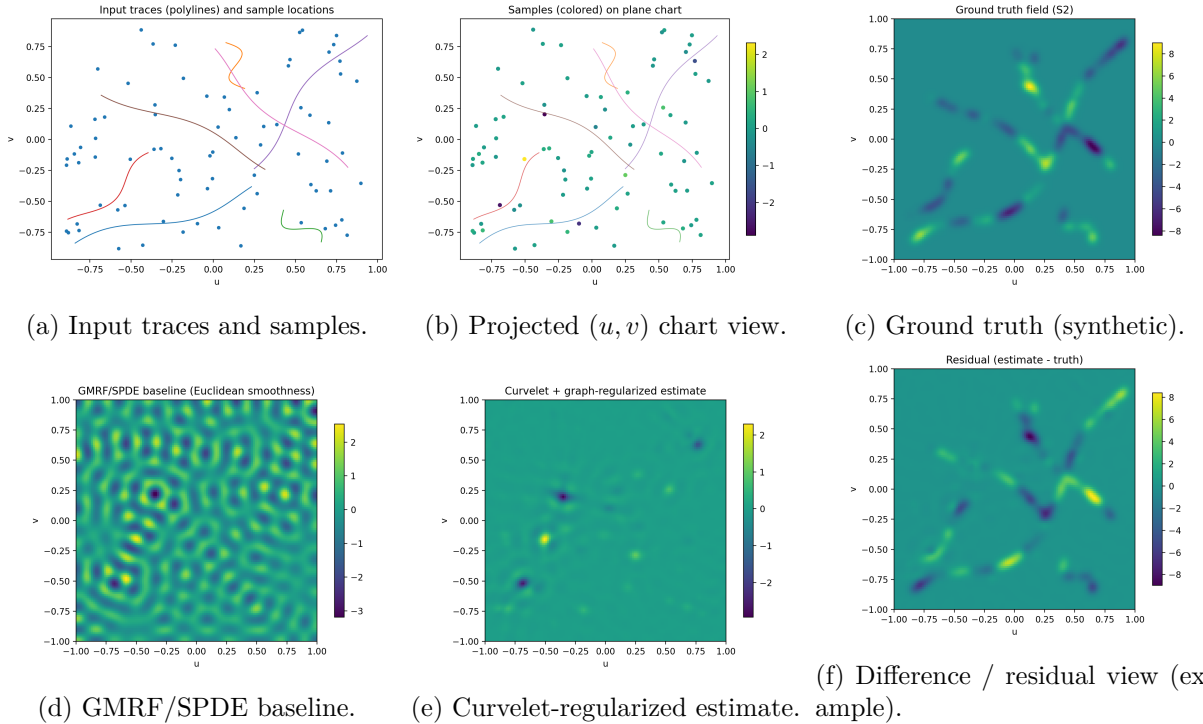


Figure 1: Representative outputs from the synthetic pipeline. Panels illustrate how the observation geometry (traces + sparse samples) and the reconstruction differ under GMRF smoothing versus curvelet-regularized recovery.

Gaussian baseline. Solving $(H^\top WH + Q)z = b$ by sparse Cholesky is efficient for grid-like sparsity; iterative CG costs $O(k \text{ nnz}(A))$ for k iterations.

Curvelet-ADMM. Each ADMM iteration performs one linear solve with $A = H^\top WH + Q + \rho I$ plus one forward and one inverse curvelet transform. For typical implementations, the transform cost is $O(M \log M)$ [3]. Thus $T_{\text{iter}} \approx T_{\text{solve}} + O(M \log M)$. Peak memory is $O(M)$ plus coefficient storage determined by transform redundancy.

13 Use Cases

Hydrogeology and transport. Plane-restricted $\log T$ or tracer concentration fields informed by mapped fractures and sparse tests/measurements [1, 19].

Geothermal stimulation and reservoir monitoring. Permeability enhancement proxies and thermal fronts aligned with fracture corridors.

Mining geomechanics and rock mass characterization. Damage/intensity fields on dominant structures combining mapped traces (photogrammetry/LiDAR) and sparse point proxies.

Geophysical surface imaging. Seismic attribute or amplitude reconstructions on mapped surfaces; curvelets are known to sparsify wavefront-like features [13, 12].

Table 2: Quantitative comparison on synthetic benchmarks (mean \pm std over seeds 0–4; $n = 128$, $N = 80$ samples; ADMM $K = 16$). Metrics are computed on a held-out 20% subset against noise-free truth at those locations.

Benchmark	Method	RMSE (hold-out)	R^2 (hold-out)	Notes
S1	Ordinary kriging	1.26 ± 0.23	-0.59 ± 1.12	RBF-kernel surrogate in code
S1	GMRF/SPDE	1.83 ± 0.33	-2.97 ± 4.28	Euclidean (u, v) smoothness
S1	+ Curvelets	1.15 ± 0.30	-0.12 ± 0.35	directional sparsity (transform pr)
S2	Ordinary kriging	1.25 ± 0.60	-2.21 ± 2.16	struggles on graph-driven truth
S2	GMRF/SPDE	1.07 ± 0.40	-1.40 ± 1.38	Euclidean (u, v) smoothness
S2	+ Graph prior	0.96 ± 0.52	-0.55 ± 0.43	along-fracture connectivity prior
S2	+ Curvelets + Graph prior	0.78 ± 0.40	-0.04 ± 0.07	full model

14 Limitations and Roadmap

- **Planar approximation:** real fractures may be rough or curved surfaces; Version 1 targets dominant planes as a tractable start.
- **Partial traces:** surface traces may not capture subsurface connectivity; Version 2 uses graphs and intersection coupling to strengthen structure.
- **Nonlinear physics:** transport/flow may require PDE-based forward models; this framework is designed to be coupled to such models.
- **Parameter tuning:** (κ, λ, ρ) require calibration; we provide a reproducible selection strategy and sensitivity analysis plan.

15 Conclusion

We presented a framework for fractured-media geostatistics that (i) uses 3D trace polylines to infer fracture planes and construct per-plane charts, (ii) reconstructs plane fields from sparse samples using a Gaussian SPDE/GMRF baseline, and (iii) promotes fracture-aligned structure via curvelet sparsity solved by ADMM with standard convergence guarantees. We formalized the “along-fracture distance” principle using graph Laplacians and a plane–graph coupling term, and provided a publication-ready validation protocol (benchmarks, metrics, baselines, ablations, sensitivity, and scaling). This establishes a concrete and extensible starting point for network-aware geostatistics in fractured media.

Data and Code Availability

A reference implementation is available as a Python prototype.

References

[1] B. Berkowitz. Characterizing flow and transport in fractured geological media: A review. *Advances in Water Resources*, 25(8–12):861–884, 2002.

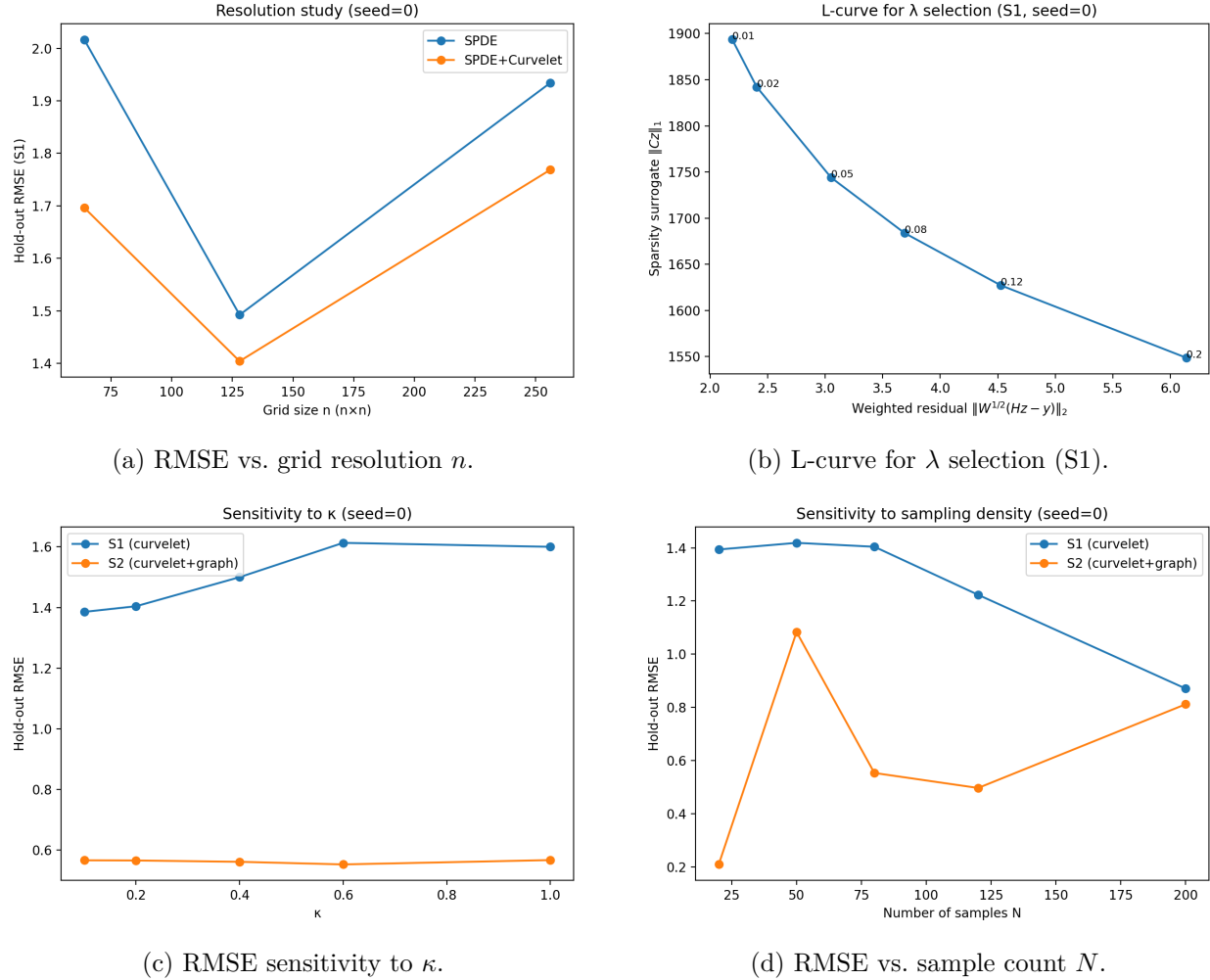


Figure 2: Sensitivity and resolution diagnostics for the synthetic benchmarks (Section 11). Panel (a) supports the choice of $n = 128$ as a cost–accuracy compromise; panel (b) illustrates the residual–sparsity trade-off for λ ; panels (c–d) characterize robustness to κ and to sampling density.

- [2] S. Boyd, N. Parikh, E. Chu, B. Peleato, and J. Eckstein. Distributed optimization and statistical learning via the alternating direction method of multipliers. *Foundations and Trends in Machine Learning*, 3(1):1–122, 2011.
- [3] E. J. Candès, L. Demanet, D. L. Donoho, and L. Ying. Fast discrete curvelet transforms. *Multiscale Modeling & Simulation*, 5(3):861–899, 2006.
- [4] E. J. Candès and D. L. Donoho. Ridgelets: a key to higher-dimensional intermittency? *Philosophical Transactions of the Royal Society of London. Series A*, 357(1760):2495–2509, 1999.
- [5] E. J. Candès and D. L. Donoho. Curvelets—a surprisingly effective nonadaptive representation for objects with edges. In *Curves and Surfaces* (Saint-Malo 1999), Vanderbilt University Press, 2000.

- [6] E. J. Candès and D. L. Donoho. New tight frames of curvelets and optimal representations of objects with piecewise C^2 singularities. *Communications on Pure and Applied Mathematics*, 57(2):219–266, 2004.
- [7] J.-P. Chilès and P. Delfiner. *Geostatistics: Modeling Spatial Uncertainty* (2nd ed.). Wiley, 2012.
- [8] F. R. K. Chung. *Spectral Graph Theory*. American Mathematical Society, 1997.
- [9] N. Cressie. *Statistics for Spatial Data* (Revised ed.). Wiley, 1993.
- [10] J.-R. de Dreuzy, P. Davy, and O. Bour. Hydraulic properties of two-dimensional random fracture networks following a power law length distribution: 1. Effective connectivity. *Water Resources Research*, 37(8):2065–2078, 2001.
- [11] W. S. Dershowitz and H. H. Einstein. Characterizing rock joint geometry with joint system models. *Rock Mechanics and Rock Engineering*, 21:21–51, 1988.
- [12] F. J. Herrmann, G. Hennenfent, and collaborators. Curvelet-based seismic data processing: A multiscale and nonlinear approach. *Geophysics*, 73(1):A1–A5, 2008.
- [13] G. Hennenfent and F. J. Herrmann. Non-parametric seismic data recovery with curvelet frames. *Geophysical Journal International*, 173(1):233–248, 2008.
- [14] G. Kutyniok and D. Labate (eds.). *Shearlets: Multiscale Analysis for Multivariate Data*. Birkhäuser, 2012.
- [15] P. R. La Pointe and J. A. Hudson. *Characterization and Interpretation of Rock Mass Joint Patterns*. Geological Society of America, 1985.
- [16] F. Lindgren, H. Rue, and J. Lindström. An explicit link between Gaussian fields and Gaussian Markov random fields: the stochastic partial differential equation approach. *Journal of the Royal Statistical Society: Series B*, 73(4):423–498, 2011.
- [17] S. Mallat. *A Wavelet Tour of Signal Processing: The Sparse Way* (3rd ed.). Academic Press, 2009.
- [18] National Research Council. *Rock Fractures and Fluid Flow: Contemporary Understanding and Applications*. National Academies Press, 1996.
- [19] S. P. Neuman. Trends, prospects and challenges in quantifying flow and transport through fractured rocks. *Hydrogeology Journal*, 13:124–147, 2005.
- [20] H. Rue and L. Held. *Gaussian Markov Random Fields: Theory and Applications*. Chapman & Hall/CRC, 2005.
- [21] D. I. Shuman, S. K. Narang, P. Frossard, A. Ortega, and P. Vandergheynst. The emerging field of signal processing on graphs: extending high-dimensional data analysis to networks and other irregular domains. *IEEE Signal Processing Magazine*, 30(3):83–98, 2013.
- [22] J.-L. Starck, F. Murtagh, and J. M. Fadili. *Sparse Image and Signal Processing: Wavelets, Curvelets, Morphological Diversity*. Cambridge University Press, 2010.
- [23] H. Wackernagel. *Multivariate Geostatistics: An Introduction with Applications* (3rd ed.). Springer, 2003.

- [24] T. T. Nguyen and H. Chauris. Uniform discrete curvelet transform. *IEEE Transactions on Signal Processing*, 58(7):3618–3634, 2010.
- [25] F. Delay and J. Bodin. Time domain random walk method to simulate transport by advection-dispersion and matrix diffusion in fracture networks. *Geophysical Research Letters*, 28(21):4051–4054, 2001.
- [26] M. V. Afonso, J. M. Bioucas-Dias, and M. A. T. Figueiredo. An augmented Lagrangian approach to the constrained optimization formulation of imaging inverse problems. *IEEE Transactions on Image Processing*, 20(3):681–695, 2011.
- [27] Chilès, J.-P. and de Marsily, G. (1993). Geostatistics for natural resources characterization. In *Statistics for the Environment*, Wiley, pp. 83–96.
- [28] Dershowitz, W. S., LaPointe, P., Eiben, T., and Wei, L. (2004). Integration of discrete feature network methods with conventional simulator approaches. *SPE Reservoir Evaluation & Engineering*, 7(02):165–170.
- [29] Hammond, D. K., Vanderghenst, P., and Gribonval, R. (2011). Wavelets on graphs via spectral graph theory. *Applied and Computational Harmonic Analysis*, 30(2):129–150.